

Cite this: *J. Mater. Chem. A*, 2013, **1**, 8209

## Bicrystalline $\text{TiO}_2$ with controllable anatase–brookite phase content for enhanced $\text{CO}_2$ photoreduction to fuels†

Huilei Zhao,<sup>a</sup> Lianjun Liu,<sup>a</sup> Jean M. Andino<sup>bc</sup> and Ying Li<sup>\*a</sup>

Among the three naturally existing phases of  $\text{TiO}_2$ , brookite is the least studied as a photocatalyst. In this study, single-phase anatase and brookite, and mixed-phase anatase–brookite  $\text{TiO}_2$  nanomaterials were synthesized through a hydrothermal method. The anatase–brookite phase content was controlled by adjusting the concentration of urea in the precursor solution. XRD, Raman spectroscopy, and high-resolution TEM were used to confirm the crystal structures. SEM and TEM analyses demonstrated that anatase  $\text{TiO}_2$  were nearly spherical nanoparticles while brookite  $\text{TiO}_2$  were rod-shaped nanoparticles. UV-vis diffuse reflectance spectroscopy showed a blue shift in absorption spectra with increasing brookite content. The photocatalytic activities of the prepared bicrystalline  $\text{TiO}_2$  were evaluated for  $\text{CO}_2$  photoreduction in the presence of water vapor for production of solar fuels (CO and  $\text{CH}_4$ ). The activities were compared with those of pure anatase, pure brookite, and a commercial anatase–rutile  $\text{TiO}_2$  (P25). The results showed that bicrystalline anatase–brookite was generally more active than single-phase anatase, brookite, and P25. The bicrystalline mixture with a composition of 75% anatase and 25% brookite showed the highest photocatalytic activity, likely due to the enhanced interfacial charge transfer between anatase and brookite nanocrystals. *In situ* DRIFTS analysis showed that  $\text{CO}_2^-$  and  $\text{HCO}_3^-$  species were active reaction intermediates for  $\text{CO}_2$  photoreduction while the accumulation of non-reactive  $\text{CO}_3^{2-}$  species on the  $\text{TiO}_2$  surface may be detrimental.

Received 26th March 2013

Accepted 25th May 2013

DOI: 10.1039/c3ta11226h

[www.rsc.org/MaterialsA](http://www.rsc.org/MaterialsA)

### 1 Introduction

The conversion of solar energy into fuels using  $\text{CO}_2$  as the feedstock by photocatalysts such as  $\text{TiO}_2$  offers significant promise in the development of a sustainable energy technology. The general products from  $\text{CO}_2$  photoreduction by  $\text{TiO}_2$  photocatalysts are CO,  $\text{CH}_4$ ,  $\text{CH}_3\text{OH}$ ,  $\text{HCOOH}$ , etc.<sup>1–4</sup> However, the well-known large band gap of  $\text{TiO}_2$  and the fast recombination rate of the photogenerated electrons ( $e^-$ ) and holes ( $h^+$ ) have limited the development of solar fuel technology. Modifications of  $\text{TiO}_2$  by metal deposition or non-metal doping have been attempted to improve the  $\text{CO}_2$  conversion efficiency.<sup>1,5</sup>

Anatase, brookite, and rutile are naturally existing  $\text{TiO}_2$  polymorphs.<sup>6–9</sup> Anatase based catalysts have been demonstrated to be highly active, while rutile is less active,<sup>10,11</sup> mainly due to the fast  $e^-$  and  $h^+$  recombination in rutile.<sup>12</sup> Mixtures of anatase–

rutile such as commercially available  $\text{TiO}_2$  nanopowder, Evonik P25 (approximately 75% anatase and 25% rutile) have demonstrated higher photocatalytic activity than single-phase anatase or rutile crystals in various photocatalytic applications.<sup>13,14</sup> Brookite is rarely studied in photocatalysis likely due to the past difficulties in synthesizing high purity brookite because of its metastable property.<sup>15–18</sup> A few studies demonstrated the high activity of brookite in photocatalytic oxidation applications.<sup>19,20</sup> Our recent study<sup>4</sup> was the first one to investigate the activity of pure brookite  $\text{TiO}_2$  for  $\text{CO}_2$  photoreduction with water; brookite showed higher activity than rutile, and surface-defective brookite was even more active than anatase.

Mixed-phase  $\text{TiO}_2$  nanomaterials other than commercial P25  $\text{TiO}_2$  nanoparticles are scarcely studied in  $\text{CO}_2$  photoreduction, and the interactions of the different phases during the  $\text{CO}_2$  photoreduction reactions have not been explored. It is believed that the junctions between different phases of  $\text{TiO}_2$  play a significant role in improving its photo-oxidation activity.<sup>6,7</sup> Several studies have explored the mechanism for the enhanced activity of anatase and rutile mixtures such as P25; however, the findings are not conclusive. Some studies suggested that photoinduced electrons tend to transfer from the higher-level anatase conduction band (CB) to the lower-level rutile CB,<sup>21</sup> while the holes in the anatase valance band (VB) could migrate to the rutile VB.<sup>11</sup> On the

<sup>a</sup>Mechanical Engineering Department, University of Wisconsin-Milwaukee, 3200 N Cramer St, Milwaukee, Wisconsin, USA. E-mail: liying@uwm.edu; Fax: +1-414-229-6958; Tel: +1-414-229-3716

<sup>b</sup>Chemical Engineering, Arizona State University, USA

<sup>c</sup>Civil, Environmental, and Sustainable Engineering, Arizona State University, USA

† Electronic supplementary information (ESI) available: Detailed description of the Rietveld refinement of the XRD data, and the investigation of the effect of catalyst mass on the photocatalytic activity. See DOI: 10.1039/c3ta11226h



contrary, other studies suggested that electrons transfer from rutile to anatase.<sup>12,13,22,23</sup> Among them, Hurum *et al.*<sup>12,13</sup> used electron paramagnetic resonance (EPR) spectroscopy to monitor the direction of electron migration; they suggested that electrons transfer from rutile to anatase because the energy levels of the electron trapping sites in anatase are lower than that of the rutile CB. In addition, the interfacial sites between anatase and rutile facilitate the electron transport and prevent the recombination of  $e^-$  and  $h^+$ .<sup>12,13</sup> However, some recent studies reported that there are no interactions between the two phases in P25, and anatase and rutile independently catalyze reactions.<sup>24</sup>

Analogous to anatase–rutile mixed-phase  $TiO_2$ , anatase–brookite heterojunctions are expected to enhance charge separation as well, probably even superior to anatase–rutile. Possible reasons are: (1) our previous study<sup>4</sup> has discovered that brookite itself is more active than rutile in  $CO_2$  photoreduction; (2) the CB edge of brookite is slightly above that of anatase,<sup>25</sup> making it possible for electrons to transfer from brookite to anatase even in the absence of anatase trapping sites. Some experimental evidence exists in the literature indicating that anatase–brookite mixtures are more active than anatase–rutile mixtures (*e.g.* P25)<sup>26</sup> and pure anatase<sup>7,27</sup> for photo-oxidation of organic compounds. While bicrystalline anatase–brookite  $TiO_2$  has demonstrated certain promising photocatalytic oxidation abilities, the relationship between phase composition and catalytic activity is not clear. In the case of anatase and rutile mixtures, there is an optimum phase content (*i.e.*, anatase–rutile = 77/23) that corresponds to the highest photoactivity.<sup>28,29</sup> The optimum phase composition in an anatase–brookite has never been explored; moreover, no studies have been reported on its application in  $CO_2$  photoreduction and the correlation of material properties with photocatalytic activities.

In this work, we have synthesized pure phase anatase, brookite, and mixed-phase anatase–brookite catalysts with a controllable brookite fraction. For the first time in the literature, we have investigated and report the effect of  $TiO_2$  phase fractions and nanostructures on  $CO_2$  photoreduction, including the optimum phase composition for  $CO_2$  photoreduction. We have also conducted *in situ* spectroscopic studies to investigate the  $CO_2$  reduction mechanism.

## 2 Experiments

### 2.1 Catalyst preparation

$TiO_2$  nanocrystals of single-phase anatase and brookite and mixed-phase anatase–brookite were prepared using a

hydrothermal method.<sup>19</sup> In a typical preparation process, 10 ml titanium bis(ammonium lactate)dihydroxide (50% in  $H_2O$ , Sigma-Aldrich), was mixed with 90 ml urea solution (with varying concentration of urea) and sealed in a 250 ml Teflon-lined autoclave, which was then sealed and placed in an electric oven at 160 °C for 24 h. After the hydrothermal process, the autoclave was naturally cooled down to room temperature. The precipitates were centrifuged, washed with de-ionized water, dried at 60 °C for 12 h, grinded and finally calcined at 400 °C for 3 h. To prepare pure phase anatase, the urea concentration in the precursor solution was 0.1 M. A urea concentration above 0.1 M led to the formation of an anatase–brookite mixture, and the brookite content increased with the urea concentration. At 7.0 M, pure brookite was formed. Table 1 summarizes the relation between the urea concentration and the phase composition. The prepared  $TiO_2$  mixtures were denoted as  $A_xB_y$ , where  $x$  and  $y$  are the phase fraction of anatase and brookite, respectively.

### 2.2 Catalyst characterization

The crystal structures of the prepared  $TiO_2$  samples were identified by X-ray diffraction (Scintag XDS 2000) using  $Cu K\alpha$  irradiation at 45 kV and a diffracted beam monochromator operated at 40 mA in the  $2\theta$  range from 20° to 50° at a scan rate of 2° min<sup>-1</sup>. The crystallite sizes of catalysts were calculated by the Scherrer equation. Quantitative phase composition analysis of as prepared  $TiO_2$  was performed using Rietveld refinement method by the MAUD software (version 2.33).<sup>30,31</sup> The XRD data of as prepared  $TiO_2$  samples together with the known standard data of anatase (tetragonal) and brookite (orthorhombic) were loaded into the MAUD software. The isotropic model and anisotropic model were chosen for anatase and brookite, respectively.<sup>30</sup> Peak positions and scale factors were adjusted before quantitative analysis.

Raman spectroscopy was carried out with a Renishaw 1000B system in the range of 100–700 cm<sup>-1</sup>. The specific surface areas of all synthesized catalysts were obtained by nitrogen adsorption–desorption at 77 K using the Brunauer–Emmett–Teller (BET) method (Micrometrics, ASAP 2020). UV-vis spectra of the catalysts were obtained by a diffuse reflectance UV-vis spectrophotometer (Ocean Optics) using  $BaSO_4$  as the background. The morphologies of  $TiO_2$  polymorphs were characterized by scanning electron microscopy (SEM, Hitachi S4800), using a secondary electron detector (SE) at an accelerating voltage range of 5–10 kV. Transmission electron microscopy (TEM) and high-resolution transmission electron microscopy (HRTEM) were carried out

**Table 1** The characteristics of prepared  $TiO_2$  catalysts including crystal phase content, BET specific surface area, pore size and pore volume, band gap, and the corresponding urea concentration in the precursor solution during material synthesis

Catalyst	Urea conc. (M)	Anatase phase (%)	Brookite phase (%)	BET specific surface area (m <sup>2</sup> g <sup>-1</sup> )	Pore size (nm)	Pore volume (cm <sup>3</sup> g <sup>-1</sup> )	Band gap (eV)
A <sub>100</sub>	0.1	100	0	145.6	6.2	0.23	3.08
A <sub>96</sub> B <sub>4</sub>	0.25	96	4	134.5	5.9	0.20	3.12
A <sub>75</sub> B <sub>25</sub>	0.5	75	25	140.3	5.5	0.20	3.15
A <sub>50</sub> B <sub>50</sub>	1.0	50	50	84.5	7.0	0.18	3.15
A <sub>37</sub> B <sub>63</sub>	1.5	37	63	70.2	10.7	0.19	3.20
B <sub>100</sub>	7.0	0	100	76.6	18.4	0.35	3.22



with 300 keV electrons in a Hitachi H9000NAR instrument with 0.18 nm point and 0.11 nm lattice resolutions, to obtain crystal structure, morphology, and lattice information of  $\text{TiO}_2$  nanocrystals.

### 2.3 Photocatalytic activity measurement

The photocatalytic reduction of  $\text{CO}_2$  over the  $\text{TiO}_2$  samples was conducted in a photoreactor operating in a continuous-flow mode. The experimental setup was similar to that described in our previous work.<sup>1</sup> A solar simulator (Oriel, 150 W) was used as the light source. The light intensity was  $69.6 \text{ mW cm}^{-2}$  for  $200 < \lambda < 1000 \text{ nm}$  and  $12.5 \text{ mW cm}^{-2}$  for  $200 < \lambda < 400 \text{ nm}$  (UV region), as measured by a spectroradiometer (International Light Technologies ILT950). The photoreactor was cylindrical shape with a stainless steel housing and a quartz window (dia. = 7.5 cm). For each test, 100 mg  $\text{TiO}_2$  powder catalyst was evenly dispersed onto a glass-fiber filter that was placed at the bottom of the photoreactor facing the light source. Ultrahigh purity  $\text{CO}_2$  (99.999%, Praxair) regulated by a mass-flow controller (MFC) continuously passed through a bubbler that contained deionized water. The resulting gas mixture ( $\text{CO}_2$  and 2.3 vol%  $\text{H}_2\text{O}$  vapor) was introduced to the photoreactor. A gas chromatograph (GC, Agilent 7890A) equipped with a thermal conductivity detector (TCD) and a flame ionization detector (FID) was used to continuously analyze the gaseous products. A Carboxen-1010 PLOT capillary column coupled with the TCD was used for CO measurement, and a HP-PLOT-Q capillary column coupled with the FID was used for  $\text{CH}_4$  measurement.

### 2.4 In situ DRIFTS analysis

*In situ* diffuse reflectance infrared Fourier transform spectroscopy (DRIFTS) is one of the most powerful tools to identify and characterize adsorption species and reaction intermediates on the catalyst surface; however, it is not often used in studying  $\text{CO}_2$  activation and reduction on  $\text{TiO}_2$ . In this work, *in situ* DRIFTS analysis was conducted to evaluate the interaction of  $\text{CO}_2$  and  $\text{H}_2\text{O}$  vapor with the photocatalyst surface in the dark and under photo-illumination. Detailed description of the DRIFTS setup can be found in our previous publication.<sup>4</sup> The *in situ* experiments were conducted under such a sequential procedure: (1) the catalyst was purged with He at  $200^\circ\text{C}$  to remove the residual water and hydroxyl groups on the surface, (2) a  $\text{CO}_2\text{-H}_2\text{O}$  mixture was continuously introduced to the DRIFTS cell for 30 min when the intensities of adsorption peaks of  $\text{CO}_2$  and  $\text{H}_2\text{O}$  reached saturation levels, and (3) the light from the solar simulator was introduced to the DRIFTS cell by a liquid guide. The IR spectra were recorded as a function of time to monitor the surface adsorbed species during  $\text{H}_2\text{O}$  and  $\text{CO}_2$  adsorption in the dark (step 2) and the surface intermediates during the photocatalytic reaction process (step 3).

## 3 Results and discussion

### 3.1 Crystal structure and morphology of $\text{TiO}_2$ polymorphs

The urea concentration in the precursor solution was directly related to the phase content of the prepared  $\text{TiO}_2$  nanocrystals

(Table 1). The crystal structure of  $\text{TiO}_2$  with different ratios of anatase–brookite was confirmed by XRD, as shown in Fig. 1a. The anatase–brookite ratios were calculated by the Rietveld refinement method. Fig. 1b shows the Rietveld refinement result of  $\text{A}_{50}\text{B}_{50}$  as an example. It demonstrates three important aspects about the crystal structure of  $\text{TiO}_2$ : (1) the peak positions of the fitting curve match the standard anatase and brookite peak positions nicely, which directly proved the bicrystalline  $\text{TiO}_2$  was composed of anatase and brookite mixture crystal phases; (2) the black solid fitting curve (from refinement result) and the blue dots (experimental XRD data) match very well, indicating a high goodness of fitting (GOF); and (3) the very small fluctuation of the GOF curve at the bottom indicates a high quality refinement result.<sup>32</sup> The phase ratio is calculated by the MAUD software automatically after the appropriate refinement. The Rietveld refinement results for all the bicrystalline  $\text{TiO}_2$  samples are shown in Fig. S1 to S4 in the ESI.†

At the lowest concentration of urea (0.1 M), pure phase anatase (JCPDS no. 21-1272), *i.e.*,  $\text{A}_{100}$ , was obtained. With an increasing concentration of urea up to 1.5 M, bicrystalline anatase–brookite mixtures with an increasing brookite fraction, *i.e.*,  $\text{A}_{96}\text{B}_4$ ,  $\text{A}_{75}\text{B}_{25}$ ,  $\text{A}_{50}\text{B}_{50}$ , and  $\text{A}_{37}\text{B}_{63}$  were formed. At the highest urea concentration (7.0 M), pure brookite (JCPDS no. 29-1360) was obtained. The existence of brookite in the resultant powders is readily discernible from its unique (121),

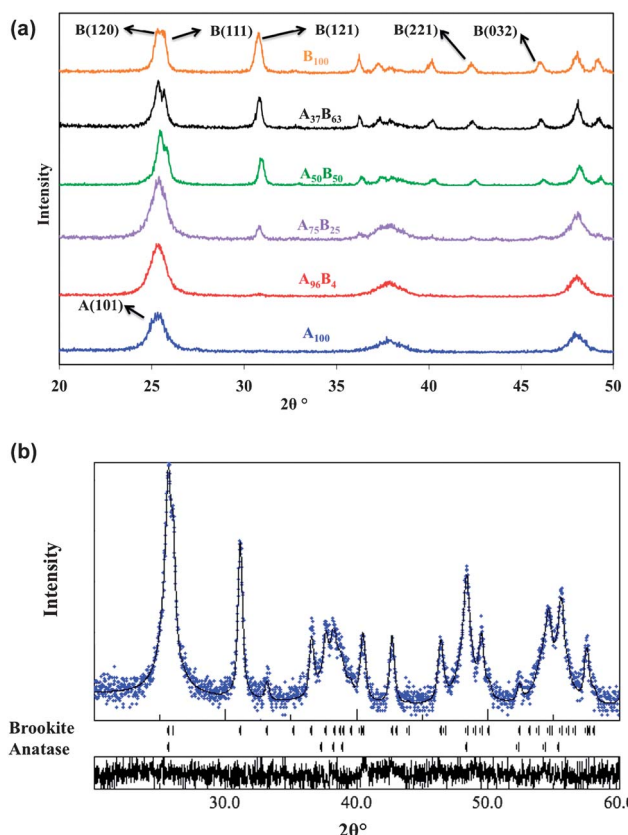
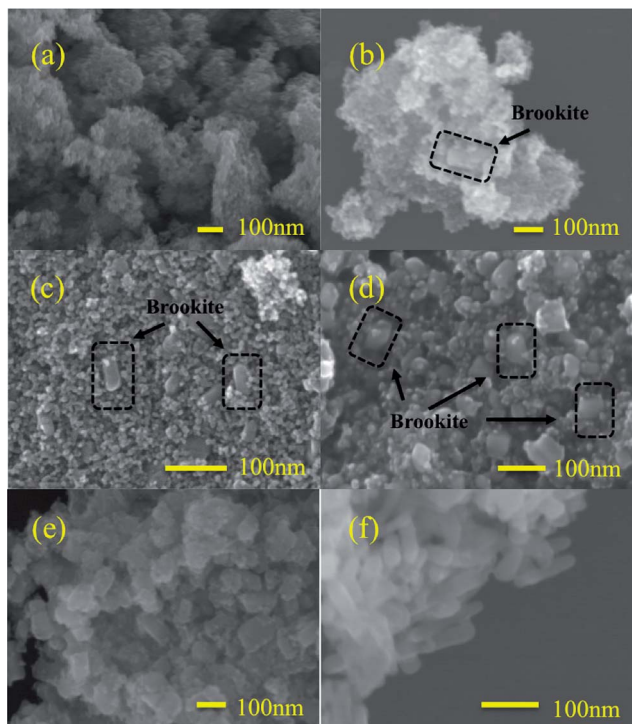


Fig. 1 XRD patterns of the prepared  $\text{TiO}_2$  catalyst powders with different fractions of anatase and brookite phases (a); Rietveld refinement result for the  $\text{A}_{50}\text{B}_{50}$  sample – solid line: fitting curve; blue dots: experimental data; bottom panel: goodness of fitting (GOF) (b).





**Fig. 2** SEM images of  $A_{100}$  (a),  $A_{96}B_4$  (b),  $A_{75}B_{25}$  (c),  $A_{50}B_{50}$  (d),  $A_{37}B_{63}$  (e), and  $B_{100}$  (f). The circled areas in black in (b), (c), and (d) indicate brookite nanobricks.

(221), and (032) diffraction peaks at  $30.81$ ,  $42.34$ ,  $46.07^\circ$  ( $\theta$ ), respectively (Fig. 1a). Clearly, through adjusting the concentration of urea, anatase, brookite or mixtures with controllable anatase–brookite phase fractions were successfully prepared.

The morphologies of the prepared  $TiO_2$  nanocrystals were examined by SEM, as shown in Fig. 2. Pure anatase,  $A_{100}$ , consisted of agglomerate sphere-shaped nanoparticles, while pure brookite,  $B_{100}$ , was rod-shaped nanoparticles. For anatase–brookite mixtures, the brookite nanorods appeared to have a lower aspect ratio (brick-shaped) than those observed in pure brookite (rod-shaped). With an increasing brookite fraction in the anatase–brookite mixtures, the number of nanobricks/nanorods increased and the size became larger. Eventually, the brookite crystals evolved from nanobricks to nanorods as the brookite content approached 100%.

The particle size, morphology, and lattice structure of  $A_{75}B_{25}$  were further evaluated by TEM and HRTEM, as shown in Fig. 3.

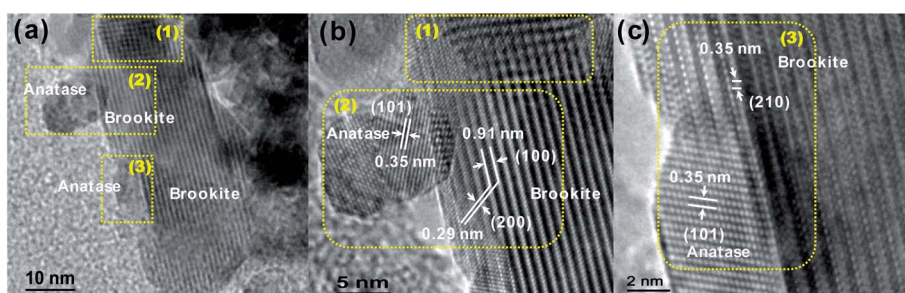
Mixtures of spherical and rod-shaped nanoparticles were observed (Fig. 3a). The spherical particles are in the range of 5–10 nm and the nanorod has a width of 20 nm and length of 60 nm. HRTEM images in Fig. 3b and c clearly demonstrated that the spherical nanoparticle was anatase (lattice spacing = 0.35 nm, corresponding to the (101) plane) and the nanorod was brookite (lattice spacing = 0.91, 0.35 nm, corresponding to (100) and (210) plane, respectively).<sup>4</sup>

Fig. 3b and c also demonstrated the overlapping anatase and brookite particles and the interface between them. In Fig. 3b the lattice fringe becomes fuzzy and even discontinued (Region 1) where the anatase and brookite crystals overlap. An anatase particle was also located at the edge of brookite (Region 2). Besides those simple attachments of anatase particles to brookite particles, a coherent interface between anatase and brookite could be formed. As shown in Fig. 3c, the lattice spacing of the anatase (101) plane matches that of the brookite (210) plane (0.35 nm) in the region where the two particles overlap (Region 3). This observation agrees with theoretical simulation results that the brookite (210) surface and the most stable anatase (101) plane have the same type of building block, and both phases may share a common boundary.<sup>33</sup> On anatase (101) all the octahedron units are closely packed, while on brookite (210) the rotated units are closely packed only along the direction.<sup>33,34</sup> This difference may cause a distortion at the interface between the two crystal phases. The HRTEM images in Fig. 3 demonstrated that when anatase and brookite nanocrystals grow in the same orientation, a unique interface between them could be possibly formed.

Raman spectra (Fig. 4) have further proved the existence of both anatase and brookite crystals in the A–B mixture ( $A_{75}B_{25}$ ). Brookite has the most intense Raman bands at  $\sim 245$ ,  $\sim 320$ ,  $\sim 399$ ,  $\sim 410$ , and  $\sim 637\text{ cm}^{-1}$ , while anatase has intense Raman bands at  $\sim 399$ ,  $\sim 519$ , and  $\sim 639\text{ cm}^{-1}$ .<sup>35</sup> As compared with the spectra of  $A_{100}$  and  $B_{100}$ , the Raman spectrum of  $A_{75}B_{25}$  included all the bands of the two crystal phases, thus indicating a mixed phase of anatase and brookite.

### 3.2 Textural and optical properties of $TiO_2$ polymorphs

Fig. 5 shows that the  $N_2$  adsorption–desorption isotherms for all the six  $TiO_2$  samples are Type IV, characteristics of materials with mesoporous structures. The isotherms of  $B_{100}$  and  $A_{37}B_{63}$  have a similar shape and close at a higher relative pressure



**Fig. 3** TEM images of  $A_{75}B_{25}$  (a), and HRTEM images of  $A_{75}B_{25}$  (b and c).



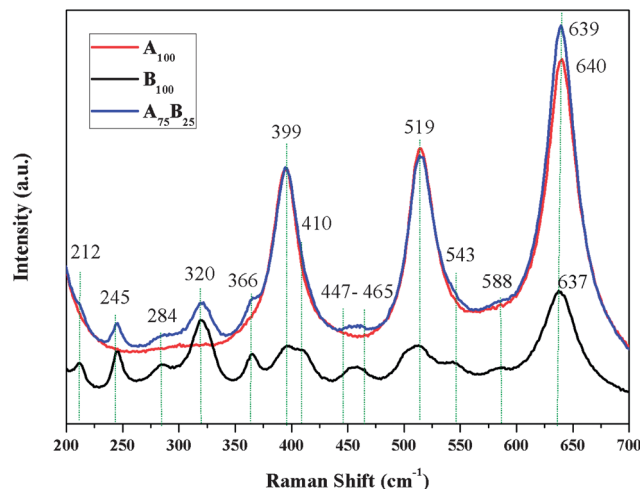


Fig. 4 Raman spectra of  $A_{100}$ ,  $B_{100}$ , and  $A_{75}B_{25}$  samples.

compared to those of  $A_{100}$ ,  $A_{96}B_4$ ,  $A_{75}B_{25}$ , and  $A_{50}B_{50}$ . Correspondingly, the calculated pore sizes of anatase-rich  $TiO_2$  are smaller than those of brookite-rich  $TiO_2$  (Table 1). This is because the inter-particle spaces between the agglomerated anatase  $TiO_2$  nanoparticles were smaller than those between the

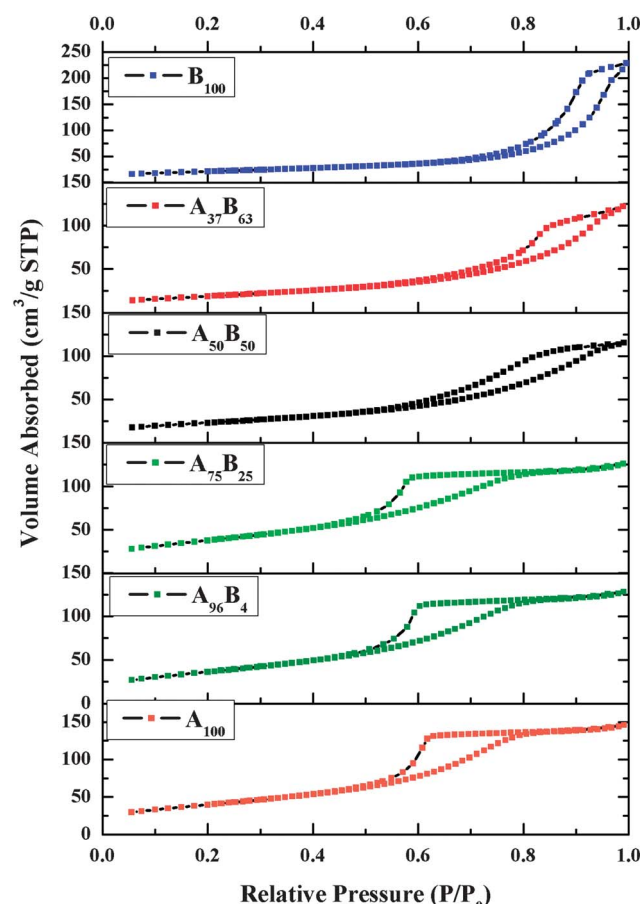


Fig. 5 Nitrogen adsorption–desorption isotherms for the prepared  $TiO_2$  catalysts.

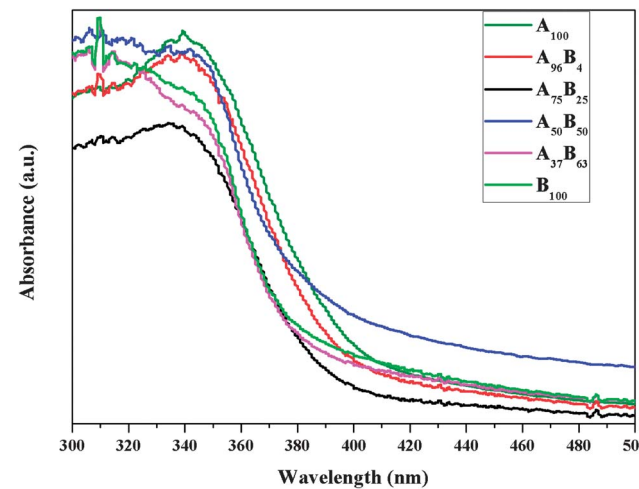


Fig. 6 The UV-vis diffuse reflectance spectra (displayed in absorbance) of the prepared  $TiO_2$  catalysts.

nanobricks/nanorods in brookite-rich  $TiO_2$ . Table 1 also compared the BET specific surface areas of the various  $TiO_2$  catalysts. The surface areas of anatase and anatase-rich samples ( $A_{100}$ ,  $A_{96}B_4$ , and  $A_{75}B_{25}$ ) were close (around  $140\text{ m}^2\text{ g}^{-1}$ ) and were twice as much as those of brookite-rich and pure brookite  $TiO_2$  ( $A_{37}B_{63}$  and  $B_{100}$ ). The sharp decrease in surface area from  $A_{75}B_{25}$  to  $A_{50}B_{50}$  can be explained from their SEM images in Fig. 2: for  $A_{75}B_{25}$ , brookite nanobricks are embedded in agglomerated anatase nanoparticles; whereas, for  $A_{50}B_{50}$ , a smaller amount of anatase nanoparticles are dispersed on the surfaces of brookite nanobricks. The surface area of the larger brookite crystals is smaller than that of the smaller anatase crystals.

Fig. 6 compares the UV-vis spectra, displayed in absorbance units, of the prepared  $TiO_2$  catalysts. The absorption edge of  $A_{100}$  is around 402 nm, corresponding to a band gap at 3.08 eV, close to the value reported in the literature.<sup>4,36</sup> An increase in the brookite fraction in the anatase–brookite mixture results in a blue shift in the absorption spectra and an increase in the band gap (listed in Table 1).  $B_{100}$  has the largest band gap at 3.22 eV. The observed larger band gap of brookite than anatase agrees with that reported in the literature,<sup>19</sup> as the conduction band of brookite is positioned at 0.14 eV more negative than that of anatase.<sup>37</sup> The catalysts after  $CO_2$  photoreduction experiments were also characterized by UV-vis, and no changes in the catalyst band gap were observed.

### 3.3 Photocatalytic activity for $CO_2$ reduction

The photocatalytic activities of the prepared  $TiO_2$  catalysts were tested for  $CO_2$  photoreduction with  $H_2O$  vapor. Background experiments were first conducted under the following conditions: (1) blank glass-fiber filter in the reactor without loading catalysts under the irradiation of solar simulator in a  $CO_2 + H_2O$  flow; (2) catalysts loaded on a glass-fiber filter in the dark in a  $CO_2 + H_2O$  flow; and (3) catalysts loaded on a glass-fiber filter under simulated solar radiation in a  $He + H_2O$  flow. In all cases, no carbon-containing products were detected. These



background tests indicated that any carbon-containing products formed (described in the subsequent part of this paper) were generated solely from the reaction of  $\text{CO}_2 + \text{H}_2\text{O}$  over the photocatalysts under light irradiation, not from any surface impurities on the catalysts.

As consistent with our previous studies,<sup>4,5</sup> CO was the major product and  $\text{CH}_4$  was the minor product formed during  $\text{CO}_2$  photoreduction with  $\text{H}_2\text{O}$  vapor, and no other products (such as  $\text{H}_2$ ) were detected. The absence of  $\text{H}_2$  production was consistent with the literature that  $\text{H}_2$  production is prominent only in the presence of noble metal co-catalysts (*e.g.*, Pt, Ag)<sup>1,38</sup> or in the presence of sacrificial agents (*e.g.*,  $\text{CH}_3\text{OH}$ ).<sup>1,39</sup>  $\text{CH}_4$  production was much lower than CO production, likely because the formation of  $\text{CH}_4$  requires the complete reduction of  $\text{CO}_2$  to C, and a subsequent reaction with available H atoms from the decomposition of water vapor on the same catalyst surface. If the CO desorbs from the surface before it can be fully reduced, then the formation of  $\text{CH}_4$  is impacted.

Fig. 7 compares the production rates of CO on various  $\text{TiO}_2$  catalysts. For each test 100 mg of catalyst was used (see Fig. S5 in the ESI† regarding the additional experiments using different amount of catalysts and the justification of using 100 mg to study the intrinsic catalyst activity). The test for each sample was repeated twice (a fresh catalyst was used each time), and the errors were within reasonable experimental uncertainties. The  $\text{CH}_4$  production rates are not plotted in Fig. 7 because they were too low (less than  $0.005 \mu\text{mol h}^{-1}$ ) and did not vary significantly for different catalysts.  $\text{B}_{100}$  had the lowest activity among all the catalysts, with a CO production rate at  $0.07 \mu\text{mol h}^{-1}$ .  $\text{A}_{100}$  had a CO production rate at  $0.12 \mu\text{mol h}^{-1}$ , higher than that of  $\text{B}_{100}$ . The bicrystalline samples with dominating anatase phase ( $\text{A}_{96}\text{B}_4$  and  $\text{A}_{75}\text{B}_{25}$ ) or equal anatase–brookite content ( $\text{A}_{50}\text{B}_{50}$ ) were the most active ones, having a CO production rate from  $0.16$  to  $0.21 \mu\text{mol h}^{-1}$ . The activity of  $\text{A}_{75}\text{B}_{25}$  was nearly twice as high as that of  $\text{A}_{100}$  and three times as high as that of  $\text{B}_{100}$ . Further increasing the brookite content (*i.e.*, brookite-rich  $\text{A}_{37}\text{B}_{63}$ ) led to a lower CO production rate at  $0.12 \mu\text{mol h}^{-1}$ .

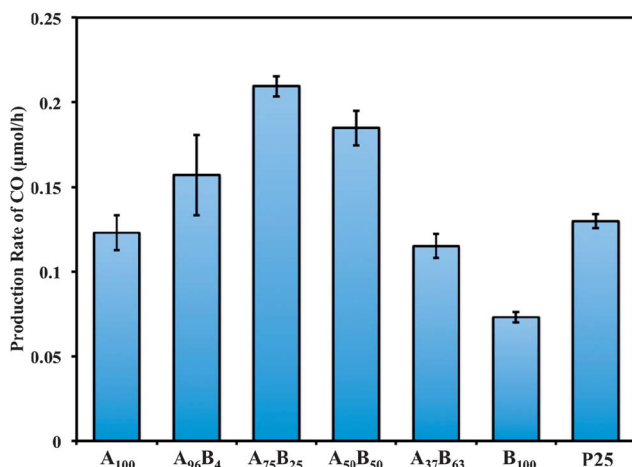


**Fig. 7** The production rates of CO using various  $\text{TiO}_2$  catalysts (the reactants were a gas mixture of 97.7 vol%  $\text{CO}_2$  and 2.3 vol%  $\text{H}_2\text{O}$ ; 100 mg catalysts were used for each test).

Commercial  $\text{TiO}_2$  P25 was also tested as comparison; it had a CO production rate of  $0.13 \mu\text{mol h}^{-1}$ , lower than the anatase-rich bicrystalline anatase–brookite samples. The above results demonstrate that the anatase-rich bicrystalline anatase–brookite mixtures are superior to single crystalline anatase or brookite and anatase–rutile mixtures (*i.e.*, P25). Considering that pure anatase  $\text{A}_{100}$  had the largest specific surface area and the smallest band gap (Table 1), the higher activity of bicrystalline anatase–brookite is very likely ascribed to the interactions between the anatase and brookite nanocrystals. This interaction between anatase and brookite seems to be more effective than that between anatase and rutile (as in P25). In addition, it is reasonable to find that anatase-rich A–B mixtures are more active than brookite-rich A–B mixtures since pure anatase is more active than pure brookite.

The experimental results in Fig. 7 indicate that anatase rich A–B mixture with 75% anatase and 25% brookite, *i.e.*,  $\text{A}_{75}\text{B}_{25}$  is the most active among all the prepared catalysts. There are three possible reasons for its superior activity: (1) the more negative CB band of brookite may induce electron transfer from brookite to anatase, thus enhancing charge separation; (2) the facilitated formation of the intrinsic defect sites in brookite may enhance electron trapping,<sup>40</sup> and (3) the distorted interfaces between anatase and brookite crystals (as evidenced in the HRTEM images) may facilitate interfacial electron transport and prevent the recombination of electron–hole pairs.<sup>41</sup> It is also noticed from Fig. 6 that anatase-rich A–B mixtures such as  $\text{A}_{75}\text{B}_{25}$  showed less light absorption in the UV region compared to other samples; the highest photocatalytic activity of  $\text{A}_{75}\text{B}_{25}$  implies the importance of interfacial charge transfer between the A and B nanocrystals.

Additional experiments were conducted to explore the potential  $\text{O}_2$  production from  $\text{H}_2\text{O}$  oxidation using the sample of  $\text{A}_{75}\text{B}_{25}$ . Prior to the photocatalytic reaction, the photoreactor was purged with a  $\text{CO}_2$ – $\text{H}_2\text{O}$  gas mixture to eliminate the air inside the reactor. However, even after purging for a few hours, there was still background  $\text{O}_2$  (in a few hundred ppm range) together with  $\text{N}_2$  detected in the reactor effluent gas. Hence, a better indicator of  $\text{O}_2$  production by the catalyst is the volumetric ratio of  $\text{O}_2/\text{N}_2$  in the effluent gas, as also suggested in the literature and in our previous work.<sup>4,42</sup> Fig. 8 shows the  $\text{O}_2/\text{N}_2$  ratio before, during and after the photoreaction, when the reactor effluent gas was sampled every 15 min. Before turning on the light (in the dark), the  $\text{O}_2/\text{N}_2$  ratio was steady. Immediately upon photo-illumination, the  $\text{O}_2/\text{N}_2$  ratio dramatically decreased in the first 60 min and then gradually increased. The sharp decrease is probably due to the consumption of residual  $\text{O}_2$  in the reactor through the reaction with photo-generated electrons  $\text{O}_2 + \text{e}^- \rightarrow \text{O}_2^-$  and consecutive reactions.<sup>4</sup> In the meantime upon photo-illumination, the production of CO and  $\text{CH}_4$  occurred, and the rates increased to their maximum in 30 to 60 min (see Fig. S6, ESI†). This indicates that although  $\text{O}_2$  competes with  $\text{CO}_2$  for photogenerated electrons, it cannot completely block the electron transfer to  $\text{CO}_2$ , since the concentration of  $\text{CO}_2$  was several orders of magnitude higher than  $\text{O}_2$  in the reactor. The gradual increase in the  $\text{O}_2/\text{N}_2$  ratio after 60 min photo-irradiation (Fig. 8) indicates the generation of  $\text{O}_2$  through oxidation of  $\text{H}_2\text{O}$  with photogenerated holes,  $\text{H}_2\text{O} + 2\text{h}^+ \rightarrow 2\text{H}^+ + \text{O}_2$ .



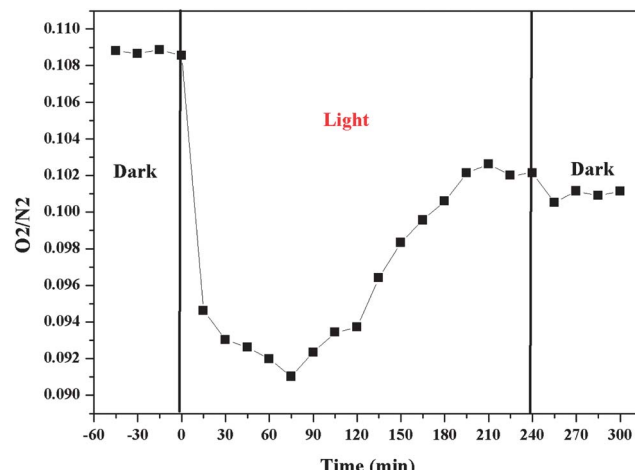


**Fig. 8** Time dependence of the volumetric ratio of  $O_2/N_2$  before, during and after the photoreduction of  $CO_2$  with  $H_2O$  on the  $A_{75}B_{25}$ .

(1/2) $O_2$ . Because the increasing amount of generated  $O_2$  outweighed the concurrent  $O_2$  consumption process, the net result was that the  $O_2/N_2$  ratio gradually increased with time and finally reached in a steady state after 200 min. After turning off the light (the second dark period), the  $O_2/N_2$  ratio dropped slightly. This result again verified the generation of  $O_2$  during the photocatalytic  $CO_2$  reduction with  $H_2O$  vapor.

#### 3.4 In situ DRIFTS investigation on surface chemistry and reaction intermediates

The lifetime of the catalysts used in this work was about 4 h, as the production rate of CO dropped to a very low level after 4 h of photo-illumination (results not shown). The short lifetime of photocatalysts (typically in the range of a few hours, if without sacrificial agents like methanol) is a well known research challenge in photoreduction applications including  $H_2$  production from water or  $CO_2$  reduction. The *in situ* DRIFTS analysis in this work is helpful to explore the surface chemistry and the reason for catalyst deactivation.

As shown in Fig. 9, in the dark,  $CO_2$ - $H_2O$  adsorption on  $A_{75}B_{25}$  resulted in the formation of bicarbonate ( $HCO_3^-$ , 1220 and 1420  $cm^{-1}$ ), bidentate carbonate ( $b-CO_3^{2-}$ , 1360 and 1570  $cm^{-1}$ ), monodentate carbonate ( $m-CO_3^{2-}$ , 1300 and 1540  $cm^{-1}$ ), and carboxylate ( $CO_2^-$ , 1250 and 1673  $cm^{-1}$ ).<sup>4,43,44</sup> The intensities of the peaks remained almost unchanged from 20 min to 30 min, indicating that the adsorption of  $CO_2$ - $H_2O$  reached the saturated level on the surface of  $A_{75}B_{25}$ . Immediately upon photo-irradiation for 15 min, the peaks for  $HCO_3^-$  and  $CO_2^-$  species decreased or even disappeared, while the peak for surface  $H_2O$  ( $1639\text{ cm}^{-1}$ )<sup>4</sup> and  $CO_3^{2-}$  increased. Upon increasing the photo-illumination time from 15 min to 3 h, the intensities of the  $H_2O$  and  $CO_3^{2-}$  peaks gradually increased, while that of  $HCO_3^-$  was gradually decreased and  $CO_2^-$  completely disappeared.

In our previous studies,<sup>45</sup> we found that  $HCO_3^-$  and  $CO_2^-$ , formed from  $CO_2$  interaction with OH groups and  $Ti^{3+}$  sites, are the possible intermediates for  $CO_2$  photoreduction to CO and  $C_1$  fuels (*e.g.*,  $CH_4$ ) once the dissociative H atom is available. The

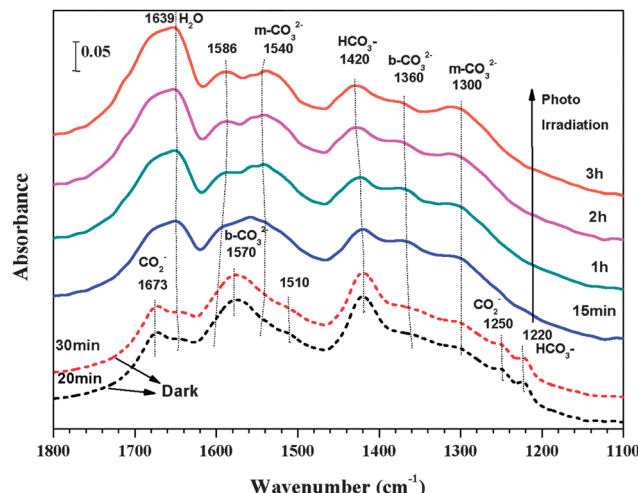


**Fig. 9** *In situ* DRIFTS spectra of  $CO_2$  and  $H_2O$  adsorption on  $A_{75}B_{25}$  for 30 min in the dark (short-dash lines), and subsequent photoreduction process under the UV-vis light irradiation for 3 h (solid lines).

DRIFTS results in Fig. 9 again demonstrated the importance of the  $HCO_3^-$  and  $CO_2^-$  as the  $CO_2$  reduction intermediates, evidenced by the weakened  $HCO_3^-$  peak and the disappearance of  $CO_2^-$  upon photo-illumination. The increase of  $CO_3^{2-}$  species could partially result from  $HCO_3^-$  transformation. The increase in surface  $H_2O$  may be explained as follows. It is known that  $H_2O$  and  $CO_2$  competitively adsorb on  $TiO_2$ .  $H_2O$  and  $CO_2$  adsorption reached equilibrium in the dark. Upon photo-illumination, this equilibrium was broken when adsorbed  $CO_2$  species was reduced to CO and desorbed into the gas phase. Hence, some surface sites like OH groups became available for incoming gas molecule adsorption. Because  $H_2O$  has a higher binding energy with surface OH groups than  $CO_2$ , once the OH groups were re-exposed, most of them may be occupied by  $H_2O$ , and thus preventing subsequent  $CO_2$  adsorption on the surface. The lack of continuous formation of active  $CO_2$  adsorption species ( $HCO_3^-$  and  $CO_2^-$ , not  $CO_3^{2-}$ ) species may cause the observed catalyst deactivation over a few hours observed in the photocatalytic activity measurements. The above described DRIFTS results have provided significant insights into the reaction mechanism and catalyst deactivation, which have been rarely studied in the literature.

## 4 Conclusions

For the first time in the literature, this paper reports the superior activity of anatase-rich anatase–brookite mixtures for the photocatalytic reduction of  $CO_2$  to fuels. The interfaces between anatase and brookite nanocrystals are believed to enhance photo-induced charge transfer and electron–hole separation, and thus they are more active than single-phase anatase or brookite. Anatase-rich A–B mixtures are more active than brookite-rich A–B mixtures since the anatase nanoparticles used in this study have higher specific surface area and smaller band gaps than the brookite nanorods that were used. The anatase-rich A–B mixture ( $A_{75}B_{25}$ ) was far more active than the



anatase-rich A–R mixture with similar anatase fraction (*i.e.* P25). This important finding suggests a new direction for the development of efficient catalysts for CO<sub>2</sub> photoreduction to fuels, *i.e.* brookite-containing mixed phase TiO<sub>2</sub> nanocrystals including tri-phasic TiO<sub>2</sub> (anatase–brookite–rutile). Our *in situ* DRIFTS analysis has demonstrated that HCO<sub>3</sub><sup>–</sup> and CO<sub>2</sub><sup>–</sup> species are important reaction intermediates for CO production. Unfortunately, the formation of those species cannot be sustained which may lead to the deactivation of the photocatalysts. Continued research in advancing the understanding of the surface chemistry is important to the design of more efficient photocatalyst in CO<sub>2</sub> reduction.

## Acknowledgements

This work was supported by National Science Foundation (CBET-1067233 and CBET-1067340).

## Notes and references

- 1 C. Y. Zhao, A. Krall, H. L. Zhao, Q. Y. Zhang and Y. Li, *Int. J. Hydrogen Energy*, 2012, **37**, 9967–9976.
- 2 Y. Izumi, *Coord. Chem. Rev.*, 2013, **257**, 171–186.
- 3 A. Dhakshinamoorthy, S. Navalon, A. Corma and H. Garcia, *Energy Environ. Sci.*, 2012, **5**, 9217–9233.
- 4 L. J. Liu, H. L. Zhao, J. M. Andino and Y. Li, *ACS Catal.*, 2012, **2**, 1817–1828.
- 5 Q. Y. Zhang, Y. Li, E. A. Ackerman, M. Gajdardziska-Josifovska and H. L. Li, *Appl. Catal., A*, 2011, **400**, 195–202.
- 6 Y. L. Liao, W. X. Que, Q. Y. Jia, Y. C. He, J. Zhang and P. Zhong, *J. Mater. Chem.*, 2012, **22**, 7937–7944.
- 7 T. Ozawa, M. Iwasaki, H. Tada, T. Akita, K. Tanaka and S. Ito, *J. Colloid Interface Sci.*, 2005, **281**, 510–513.
- 8 D. Reyes-Coronado, G. Rodriguez-Gattorno, M. E. Espinosa-Pesqueira, C. Cab, R. de Coss and G. Oskam, *Nanotechnology*, 2008, **19**, 145605.
- 9 M. Landmann, E. Rauls and W. G. Schmidt, *J. Phys.: Condens. Matter*, 2012, **24**, 195503.
- 10 G. Liu, X. W. Wang, Z. G. Chen, H. M. Cheng and G. Q. Lu, *J. Colloid Interface Sci.*, 2009, **329**, 331–338.
- 11 J. T. Carneiro, T. J. Savenije, J. A. Moulijn and G. Mul, *J. Phys. Chem. C*, 2011, **115**, 2211–2217.
- 12 D. C. Hurum, A. G. Agrios, S. E. Crist, K. A. Gray, T. Rajh and M. C. Thurnauer, *J. Electron Spectrosc. Relat. Phenom.*, 2006, **150**, 155–163.
- 13 D. C. Hurum, A. G. Agrios, K. A. Gray, T. Rajh and M. C. Thurnauer, *J. Phys. Chem. B*, 2003, **107**, 4545–4549.
- 14 Q. Zhu, J. S. Qian, H. Pan, L. Tu and X. F. Zhou, *Nanotechnology*, 2011, **22**, 395703.
- 15 V. Stengl and D. Kralova, *Mater. Chem. Phys.*, 2011, **129**, 794–801.
- 16 Q. X. Deng, M. D. Wei, Z. S. Hong, X. K. Ding, L. L. Jiang and K. M. Wei, *Curr. Nanosci.*, 2010, **6**, 479–482.
- 17 D. Dambournet, I. Belharouak and K. Amine, *Chem. Mater.*, 2010, **22**, 1173–1179.
- 18 A. Garcia-Ruiz, A. Morales and X. Bokhimi, *J. Alloys Compd.*, 2010, **495**, 583–587.
- 19 T. A. Kandiel, A. Feldhoff, L. Robben, R. Dillert and D. W. Bahnemann, *Chem. Mater.*, 2010, **22**, 2050–2060.
- 20 H. Pan, X. F. Qiu, I. N. Ivanovic, H. M. Meyer, W. Wang, W. G. Zhu, M. P. Paranthaman, Z. Y. Zhang, G. Eres and B. H. Gu, *Appl. Catal., B*, 2009, **93**, 90–95.
- 21 T. Kawahara, Y. Konishi, H. Tada, N. Tohge, J. Nishii and S. Ito, *Angew. Chem., Int. Ed.*, 2002, **41**, 2811–2813.
- 22 G. Liu, X. X. Yan, Z. G. Chen, X. W. Wang, L. Z. Wang, G. Q. Lu and H. M. Cheng, *J. Mater. Chem.*, 2009, **19**, 6590–6596.
- 23 G. H. Li, C. P. Richter, R. L. Milot, L. Cai, C. A. Schmuttenmaer, R. H. Crabtree, G. W. Brudvig and V. S. Batista, *Dalton Trans.*, 2009, 10078–10085.
- 24 B. Ohtani, O. O. Prieto-Mahaney, D. Li and R. Abe, *J. Photochem. Photobiol., A*, 2010, **216**, 179–182.
- 25 A. Di Paola, M. Bellardita, R. Ceccato, L. Palmisano and F. Parrino, *J. Phys. Chem. C*, 2009, **113**, 15166–15174.
- 26 J. C. Yu, L. Z. Zhang and J. G. Yu, *Chem. Mater.*, 2002, **14**, 4647–4653.
- 27 S. Ardizzone, C. L. Bianchi, G. Cappelletti, S. Gialanella, C. Pirola and V. Ragagni, *J. Phys. Chem. C*, 2007, **111**, 13222–13231.
- 28 S. Bakardjieva, J. Subrt, V. Stengl, M. J. Dianez and M. J. Sayagues, *Appl. Catal., B*, 2005, **58**, 193–202.
- 29 M. Boehme and W. Ensinger, *Nano-Micro Lett.*, 2011, **3**, 236–241.
- 30 H. R. Wenk, L. Lutterotti and S. C. Vogel, *Powder Diffr.*, 2010, **25**, 283–296.
- 31 M. Rezaee, S. M. M. Khoie and K. H. Liu, *CrystEngComm*, 2011, **13**, 5055–5061.
- 32 B. H. Toby, *Powder Diffr.*, 2006, **21**, 67–70.
- 33 X. Q. Gong and A. Selloni, *Phys. Rev. B: Condens. Matter Mater. Phys.*, 2007, **76**, 11.
- 34 Rashmi, N. Singh and A. K. Sarkar, *Powder Diffr.*, 2004, **19**, 141–144.
- 35 K. R. Moonoosawmy, H. Katzke, M. Es-Souni, M. Dietze and M. Es-Souni, *Langmuir*, 2012, **28**, 6706–6713.
- 36 K. Nagaveni, M. S. Hegde, N. Ravishankar, G. N. Subbanna and G. Madras, *Langmuir*, 2004, **20**, 2900–2907.
- 37 T. A. Kandiel, L. Robben, A. Alkaim and D. Bahnemann, *Photochem. Photobiol. Sci.*, 2013, **12**, 602–609.
- 38 O. K. Varghese, M. Paulose, T. J. LaTempa and C. A. Grimes, *Nano Lett.*, 2009, **9**, 731–737.
- 39 X. B. Chen, L. Liu, P. Y. Yu and S. S. Mao, *Science*, 2011, **331**, 746–750.
- 40 H. Pan, B. Gu and Z. Zhang, *J. Chem. Theory Comput.*, 2009, **5**, 3074–3078.
- 41 S. A. Wohlgemuth, R. J. White, M. G. Willinger, M. M. Titirici and M. Antonietti, *Green Chem.*, 2012, **14**, 1515–1523.
- 42 W.-N. Wang, W.-J. An, B. Ramalingam, S. Mukherjee, D. M. Niedzwiedzki, S. Gangopadhyay and P. Biswas, *J. Am. Chem. Soc.*, 2012, **134**, 11276–11281.
- 43 W. Su, J. Zhang, Z. Feng, T. Chen, P. Ying and C. Li, *J. Phys. Chem. C*, 2008, **112**, 7710–7716.
- 44 C.-C. Yang, Y.-H. Yu, B. van der Linden, J. C. S. Wu and G. Mul, *J. Am. Chem. Soc.*, 2010, **132**, 8398–8406.
- 45 L. J. Liu, C. Y. Zhao and Y. Li, *J. Phys. Chem. C*, 2012, **116**, 7904–7912.

